Wall loss dependence on strained FBG sensors' simulated response

Jean-Pierre Atanas

Abstract— Pressure vessels including pressurized pipes in the oil and gas industry are all subject to sustained load cracking and material wall loss. Constantly monitoring material wall losses at early stages is essential to the oil and gas industry. In this paper, a model of pressure wall thinning using combined FBG (Fiber Bragg Grating) sensors is presented. The simplistic model design make use of three FBG sensors, two dedicated to axial and hoop strain measurements, while the other sensor served for temperature compensation. Stress and strain simulations obtained for 1 to 5 MPa inner pipe pressures are used to identify the positions in elbows corresponding to maximum wall loss. Simulation of FBG's optical spectrum reflectivity shows a wavelength shift directly related to the thickness of the pipe material.

Index Terms— COMSOL Multphysics, FBG sensor, Fluid Flow, Fnite Element Analysis, Reflectivity Spectrum, Stress Analysis, Wall Loss

1 Introduction

Pipes and pressure vessels have been used extensively for decades to transport and store liquids and gases at high pressure. PWT (Pressure Wall Thinning) in pressure vessels or in any piping system can be produced in various mechanisms. Highly corrosive fluid carrying acid gas or petrochemicals produces in time wall thinning in carbon steel piping systems in oil and gas refineries and other industrial plants due to Flow Accelerated Corrosion (FAC) [1]. Many researchers have studied maximum allowable pressure by Finite Element Analysis (FEA) of several steel pipes, where a pipeline rehabilitation concept and reported rehabilitation of corroded pipes has been reported by putting steel back into pipelines [2], [3], [4], [5], [6]. When pipes or pipeline corrosion defect occurs, wall thinning or specifically a certain percentage of the inner wall thickness is lost and larger strains appear in the defective region under the constant pressure within the pipe [7]. Internal pressure in pipes induces longitudinal, radial and circumferential stresses. Also, an important criterion in pipe and vessel analysis is radial growth, or dilation, under internal pressure. Recently, after the discovery of fiber Bragg grating strain sensors, many researches forwarded their efforts to fiber optic design in several applications such as airspace, aircraft, civil structure, oil and gas industry and in many areas in engineering. Actually, when temperature and pressure sensing is critical, distributed temperature sensing with fiber optics is essential in many industries. Fiber optic sensing uses the fiber optic cable itself, where gratings are applied, to monitor temperature and strain across the entire length of the pipe. An important solution in such conditions would be all optic based micro-sensors for their immunity to electromagnetic interference, for the property of their material, for their ability to maintain highly safe operations in hazardous and flammable environment [8], for their low power activation and low operation cost and finally for their relatively high sensitivity and reliability. In the following sections, stress and strain analysis of pressure for straight pipes and elbows are presented. Finite element analysis is applied to elbows to derive Von Misses stress distribution and compare it with the analytical expression. A model based on a detection unit, made of the three sensors, where two of them are reserved for strain measurements and are positioned in two orthogonal directions while the third is used for temperature compensation, is being designed. Coupled-mode theory is being applied to obtain the spectral dependence of the fiber with varying effective index and different fiber grating lengths. Simulation response of the wavelength shift in reflectivity spectra, for both axial and circumferential directions, is shown and from which the expression of wall thickness is derived.

• *Jean-Pierre Atanas is currently assistant professor of physics at the Petroleum Institute, P.O. Box 2533, UAE. E-mail: jpierre@pi.ac.ae*

2 Stress Analysis of Thin Walled Pipes

2.1 Stress and strain

Pressure vessels must be able to withstand high internal pressure. An analysis study for stress and strain is considered for open ends vessels or pipes. Hoop or circumferential stress and the resulting strain are respectively given by (1) and (2), where P is the internal pressure, r the inner radius, E the Young Modulus and *t* the thickness fo the material,

$$\sigma_\theta = \frac{\mathrm{Pr}}{t} \tag{1}$$

$$\varepsilon_\theta = \frac{\mathrm{Pr}}{Et} \tag{2}$$

Axial stress is given by (3)

$$\sigma_z = \frac{\mathrm{Pr}}{2t} \tag{3}$$

Thinned-wall situations correspond to the condition where the radius is much greater than ten times pipe's wall thickness. Also, the radial stress is negligible compared to hoop and axial stresses. The maximum hoop stress in pipelines around the world is 72% S giving a design factor (ϕ = hoop stress/allowable stress = 0.72), where S is the allowable stress. Note that most pipeline codes allow overpressure of typically 10% over this maximum allowable stress; therefore, a pipeline at 72% S can experience an overpressure up to 79% S. The design factor ϕ is a safety factor and allows for variability in materials, variability in construction practices, uncertainties in loading conditions, uncertainties in service conditions. According to ASME B31.3 code committee [9], the revised Equation for deriving the nominal wall thickness of pipe reads as follows:

$$t = \frac{Pr}{\varphi \sigma_m \omega} + CA \quad (4)$$

Where the weld joint (ω) applies only at temperature above 510 degrees Celsius and is based on the effect of creep and σ_m is the minimum yield stress. In our study, temperature would be far less than the presumed one, hence, (ω = 1) unless otherwise indicated. CA denotes the sum of allowance of threading, of corrosion and of grooving. The ASME code B31.4 and ASME code B31.8 [10], [11] for liquid and gas transportation, respectively, underlines different limits on allowable longitudinal stresses for restrained and unrestrained piping. Buried pipes or similarly restrained portions under load are exposed to substantial axial restraint, which naturally are different from unrestrained or above ground portions. In the following, no additional loads are considered on the pipe except those related to internal pressure. The obtained stress and strain equations are reduced to (5) for axial stress, and (6) for hoop stress respectively.

$$\sigma_z = \alpha E \Delta T + \frac{Pr}{2t}(1-2\nu) \quad (5)$$

$$\sigma_\theta = \alpha E \Delta T + \frac{Pr}{t}(1-\frac{\nu}{2}) \quad (6)$$

Fig. 1 and 2 illustrate the surface plot of the Axial and Hoop strain versus temperature change and operational pressure for 50 mm carbon steel wall thickness and 0.534 m inner radius (42-inch pipe diameter). It is clearly shown that hoop strain is greater, for any given temperature and pressure than axial strain. These calculations were done with Matlab® and for a straight line section of the pipe. Also, hoop strain for elbows was derived and expressed as in (7),

$$\sigma_\theta = \alpha E \Delta T + \frac{Pr}{2tE}(\frac{2R + r\sin\theta}{R + r\sin\theta})(1-\frac{\nu}{2}) \quad (7)$$

Where R is the radius of curvature of the bend long tangent which is about 1.5 times the nominal pipe size according to ASME B16.9, r is the inner radius of the pipe's cross section, and θ is the angle around it.

Fig. 3 shows a cross sectional hoop strain for elbow versus internal pressure and temperature change. Highest strain is found at the inner side of the bend, hence at θ = 270 degrees from the reference direction previously defined. The zero-angle corresponds to the positive direction of the z axis represented in fig. 4. Finite Element Analysis with COMSOL Multphysics, for a single phase highly turbulent flow with the Reynolds number being around $Re \cong 5\times10^5$, was applied to the elbow to calculate Von Mises stress distribution at internal gas pressure of 1MPa, where the gas considered is assumed air for simplicity. Simulations employ the SST, k-ω turbulence model as in [14], [15]. The flow velocity at the inlet, as averaged over the pipe cross section, is assumed to be Uavg = 20 m/sec.

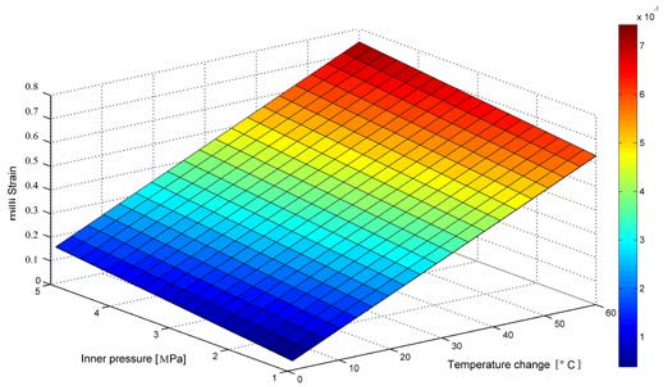

Fig. 1: Axial strain versus inner pressure and temperature change.

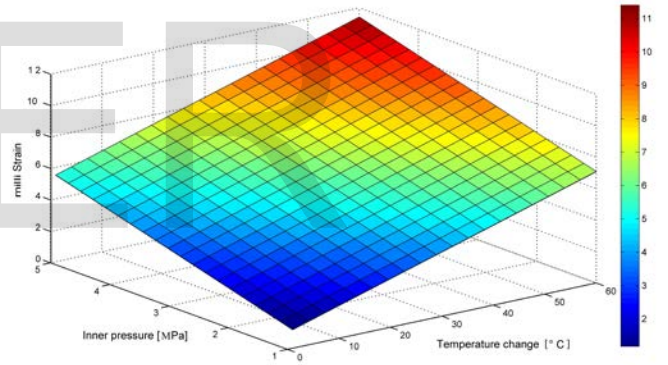

Fig. 2: Hoop strain versus inner pressure and temperature change.

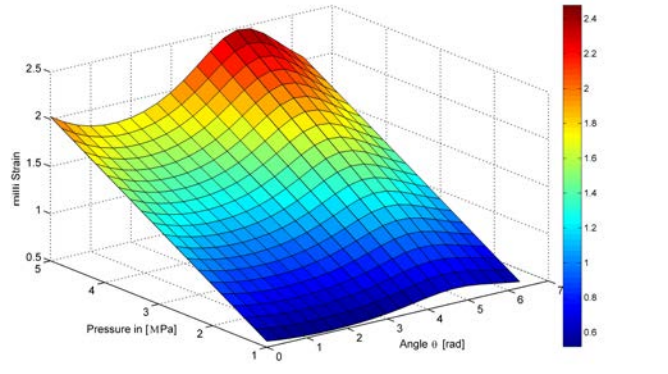

Fig. 3: Hoop strain for elbow versus inner pressure and temperature change. The angle 0 corresponds to the bottom side of the elbow and reported in radians.

No change in temperature was assumed between the inside

out of the elbow. Results are shown in Fig. 4 where maximum strain obtained at the inner bend is about 0.15 micro strains only compared to 0.5 micro strains derived from the analytical expression in (7). This difference arises from turbulence effects, gas properties and caracteristics of the fluid (density and visciosity) that were not taken into consideration in the empirical equation (7) where the pressure unrealistically is assumed constant along the cross section of the elbow.

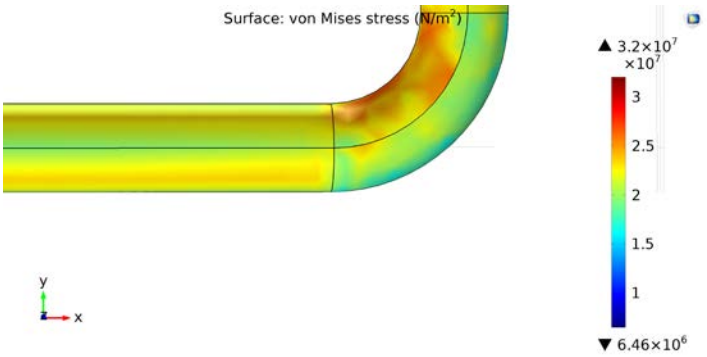

Fig. 4: COMSOL Multiphysics FEA simulation of the Von Mises stress in N/m².

2.2 Simulation of the reflectivity spectrum

Coupled-mode theory has been used to obtain quantitative information about the diffraction efficiency and spectral dependence of fiber gratings. In this paper, coupled first-order ordinary differential equations for single-mode Bragg reflection grating were solved. Details of the theory are well explained in [12], [13]. Normalized reflectivity spectra of the Bragg propagating wavelength λ = 1550 nm through the fiber optics with varying grating length L and index variation δn, were derived. A cosine apodization function has been also applied to reduce the side lobes of the reflected wave in the reflectivity spectrum so as to suppress any effect related to misdetection of the main Bragg wavelength peak. Fig. 5 shows simulation results for different length of the fiber grating, L = 5 mm, L = 10 mm and L = 20 mm, where the index of the core is n_{co} = 1.447 and that of the cladding is n_{clad} = 1.445.

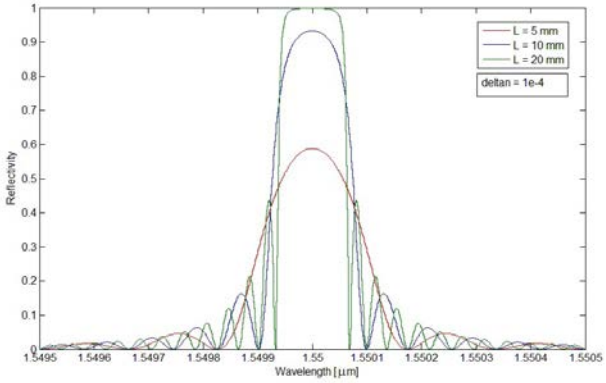

Fig. 5: Reflectivity spectrum verus length of gratings with fixed index change of 1e-4.

The calculated effective index was n_{eff} = 1.4455. In all the following sections, a grating length of L = 10 mm is assumed. It is clearly shown that the intensity of the Bragg wavelength in the reflectivity spectrum increases with the grating length L. This is to be expected, since more reflecting waves for large grating lengths will contribute more to the intensity of the reflected Bragg wavelength. However, due to some experimental constraints, the grating length are restricted to be length-specific such as other parameters could be varied such as the index change δn to compensate for the intensity decrease of the reflected Bragg wavelength. Fig. 6 shows simulation of the reflected Bragg signal for fiber grating length of L = 10 mm, while the index change δn takes respective values of 0.5e-4, 1e-4 and 2e-4.

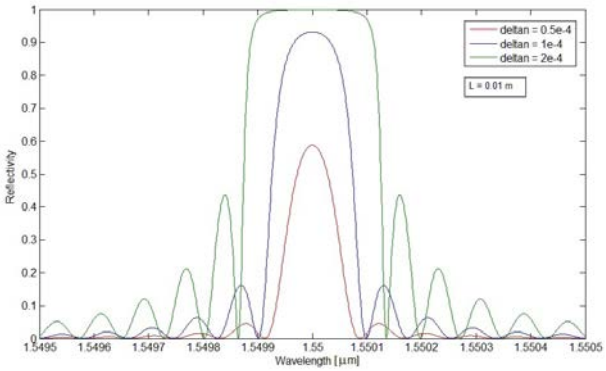

Fig. 6: Reflectivity spectrum for fixed length L=10 mm and variable index change.

It is shown that the intensity of the reflected wavelength increases with δn that is achieved by high Germanium doping of the fiber's core. Reflectivity spectra, in both Fig. 5 and 6 show side lobes around the propagating wavelength λ = 1550 nm. A way to reduce the energy spread around the main peak is to apply a cosine apodization function where fringes will be distributed periodically instead of an equal distribution around the center of the grating. The effect will be reduction of power loss at side lobes in the reflectivity spectra. Mathematically, a cosine apodization function has been applied and will be used throughout the simulation of reflectivity spectra.

2.3 Simulation of strain inducing wavelength shift

The Bragg wavelength of a grating is a function of the effective index of the guided mode n_{eff} and period of index modulation Λ. Normalized reflectivity obtained from coupled-mode theory could also be written as,

$$R(\lambda) = \frac{\sinh^2\left(\kappa L\sqrt{1-\left(\frac{\chi}{\kappa}\right)^2}\right)}{\cosh^2\left(\kappa L\sqrt{1-\left(\frac{\chi}{\kappa}\right)^2}\right)-\left(\frac{\chi}{\kappa}\right)^2} \quad (8)$$

Where L is the grating length, κ is the direct coupling coefficient, χ is the detuning parameter and χ/κ is the detuning ratio. The detuning parameter for Bragg grating of period Λ is

$$\chi = \Omega - \frac{\pi}{\Lambda} \quad (9)$$

Where the fiber core propagation is Ω = (2π n_{core}) / λ and constant at the considered wavelength. The shifted Bragg wavelength produced by the imposed strain and the temperature change is given by:

$$\Delta\lambda_B = \lambda_B(1-P_e)\Delta\varepsilon + \lambda_B(\alpha+\mu)\Delta T \quad (10)$$

Where $\Delta\lambda_B$, P_e and $\Delta\lambda$ are respectively: Bragg wavelength shift, strain optic constant and axial strain change along fiber axis. The strain optic constant is written as:

$$P_e = \frac{n_{eff}^2}{2}(P_{12} - \nu(P_{11}+P_{12})) \quad (11)$$

Fig. 7 shows Bragg wavelength shift of 3.3 nm in the simulation of the reflectivity spectrum at 2000 micro strain.

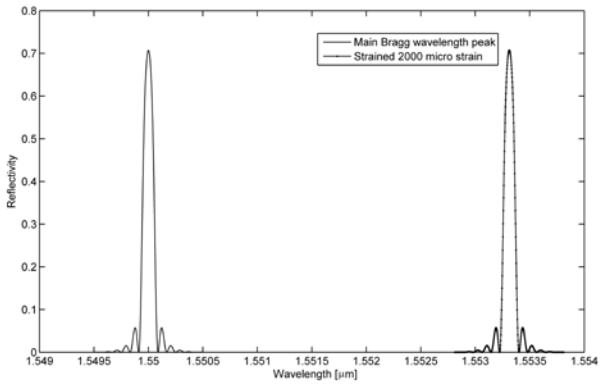

Fig. 7: Main unstrained Bragg wavelength peak vs strained peak under 200 micro strains.

The main spectrum is obtained with the following relevant parameters: Bragg wavelength $\Delta\lambda_B$ = 1550 nm, effective index n_{eff} = 1.4455, grating length L = 10 mm, grating period Λ = 532 nm, fiber optic index variation δn = 1e-4. A cosine apodization function was applied to the fiber with no local grating strength introduced. Wavelength shift illustrated in Fig. 8 shows Bragg wavelength shift for values of strain up to 3000 micro strain, and was obtained with a strain optic tensor components P_{11} = 0.113 and P_{12} = 0.252, a Poisson ratio of ν= 0.87, and thermal coefficients of α = 10.8e-6 /°C and μ = 8.6e-8/°C respectively. The wall thickness and pipe radius were respectively 50 mm and 0.5 m. Fig. 8a and 8b show a linear behavior of the wavelength shift versus temperature and strain respectively.

3 WALL LOSS DEPENDENCE OVER STRAINED FBG SENSORS

As outlined in the introduction pipeline's integrity is influenced by its surrounding environment, the transported oil or gas, the original type and state of the coating material as well as operational parameters. Cracks and wear in the pipe wall can develop from the outside, the inside or even from within the material itself. Defects can also develop during manufacturing and construction or emerge later during the operational life of the pressurized pipes or pipeline. They are marked by wall loss and thus a significant reduction in the pipe's wall thickness, hence the importance of measuring the remaining thickness of the pipe wall. A relation between pipe thickness and induced strain could be derived from the hoop strain equation as,

$$t = \frac{\Pr}{E(\varepsilon_\theta - \alpha\Delta T)}(1-0.5\nu) \quad (12)$$

Similarly, for hoop strain in elbow, we obtain,

$$t = \frac{\Pr}{E(\varepsilon_{\theta,elbow} - \alpha\Delta T)}\frac{2R + r\sin\theta}{R + r\sin\theta}(1-0.5\nu) \quad (13)$$

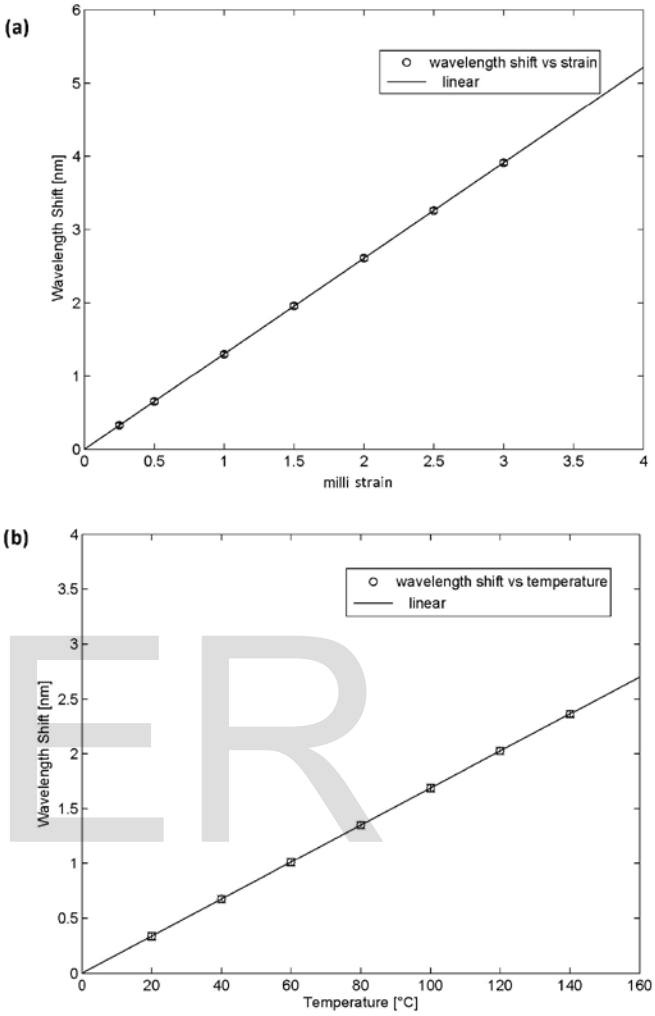

Fig. 8a and 8b: Simulated wavelength shift vs strain and temperature respectively.

Assuming a constant operational pressure of 1 MPa and 20 ℃ differential temperatures, the shift in wavelength is a direct measure of the wall loss through the above equations, since strain is directly proportional to the induced strain. Wall loss derived from the hoop strain for both straight pipe and elbow is then written respectively as in (14) and (15),

$$WL_{\theta,straight}(\Delta\lambda_B) = t_{initial} - \frac{\Pr}{E(\varepsilon_\theta - \alpha\Delta T)}(1-0.5\nu) \quad (14)$$

$$WL_{\theta,elbows}(\Delta\lambda_B) = t_{initial} - \frac{\Pr}{E(\varepsilon_\theta - \alpha\Delta T)}(1-0.5\nu) \quad (15)$$

By using temperature compensation from the temperature sensor measurement $\alpha\Delta T$ = 0, the previous wall loss expressions will be further reduced. Fig. 9 shows percent wall loss versus wavelength shift with temperature compensation and

at 1 MPa operational pressure.

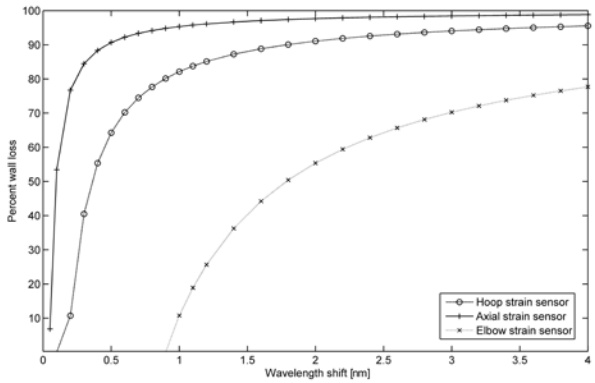

Fig. 9: Percent wall loss versus wavelength shift for straight section of pipes and elbows.

It is clear from both axial and hoop plots that one can derive the percent wall loss at any operational conditions of temperature and pressure.

5 Conclusion

Hoop and axial strain measurements for straight pipes and elbows have been developed with specific FBG sensors. The design unit is composed of two orthogonal sensors for strain measurements and one for temperature compensation. It was shown that strain is highest at the internal side of the bend for elbows and decreases with radii of curvature. The obtained relation for percent wall loss is used to monitor pipe's thickness through continuous measurement of hoop and axial strains. Percent wall loss could be monitored online by direct measurement of the wavelength shift in the reflectivity spectrum. A limit on the percent wall loss could be specified according to ASME codes to trigger repair actions for the defected parts of the pipe. FBG sensors are also known for their high multiplexing capabilities that can be used to monitor long distances of pipes or pipelines

Acknowledgment

The author wishes to thank Mr. M. Fahed for his help in setting up COMSOL Multiphysics. This work was supported in part by a grant no. 15337 from the research office at the petroleum Institute.

References

[1] K.D. Efird, "Disturbed flow and flow-accelerated corrosion in oil and gas production". J Energ Resour-Asme 120, 72-77, 1998.

[2] M. Kamaya, T. Suzuki, T. Meshii, "Failure pressure of straight pipe with wall thinning under internal pressure. International journal of pressure vessels and piping", 85, 628-634, 2008.

[3] J. Michalik, C. Kolmasiak, "Physical Modeling of Stresses during Continuous Casting of St3s Steel". Metalurgija 48, 71-74, 2009.

[4] E. Scheibner, M. Urdeq, S. Duicu, and S. Simona, "Finite element method analysis for pipeline installation systems". Metalurgia International 18, 2013.

[5] T.J.M. Bond, D.J. Miles, R.N. Burke, and N.J. Venero, "External Rehabilitation of Corroded Pipelines – Putting the Steel Back into Pipelines", Evaluation and Rehabilitation of Pipelines Conference, Pittsburgh PA, 2009.

[6] T.J.M. Bond, D.J. Miles, R.N. Burke, and N.J. Venero, "Pipeline Rehabilitation Technology for the 21st Century", 18th International Conference on Pipeline Protection, Antwerp, Belgium, 2009.

[7] M.Tomizuka, S. Kon, K. Oldham, R. Horowitz. C.B. Yun, V. Giurgiutiu, "Piezoresistive and piezoelectric MEMS strain sensors for vibration detection", Sensors and Smart Structures Technologies for Civil, Mechanical, and Aerospace Systems 6529, 65292V-65292V-65211, 2007.

[8] N.M.P Pinto, O. Frazão, J.M. Baptista, J.L. Santos, "OTDR fiber-optical chemical sensor system for detection and location of hydrocarbon leakage", Journal of Hazardous Materials, Vol. 102, Issue 1, Pages 13-28, 2003.

[9] C. Becht IV, The complete Guide to ASME B31.3, 2nd edition, process piping, 2004, American Society of Mechanical Engineers Press, New York, 2004.

[10] ASME B31.4, Pipeline transportation systems for liquid Hydro-carbons and Other Liquids, American Society of Mechanical Engineers Press, New York, 2002.

[11] ASME B31.8, Gas transmission and Distribution systems, American Society of Mechanical Engineers Press, New York. , 2003.

[12] A. Yariv, "Coupled-mode theory for guided-wave optics", IEEE J., Quantum Electron., vol. QE-9, pp. 919–933, 1973.

[13] H. Kogelnik, Theory of optical waveguides, in Guided-Wave Optoelectronics, T. Tamir, Ed. New York: Springer-Verlag, pp. 209–223 1990.

[14] F. R. Menter, "Zonal Two Equation k-ω Turbulence Models for Aerodynamic Flows", AIAA Paper 93-2906, 1993.

[15] F. R. Menter, "Two-Equation Eddy-Viscosity Turbulence Models for Engineering Applications", AIAA Journal, vol. 32, no 8. pp. 1598-1605, 1994.